

Three-Dimensional Simulations of Seismic-Wave Propagation in the Taipei Basin with Realistic Topography Based upon the Spectral-Element Method

by Shiann-Jong Lee, How-Wei Chen, Qinya Liu*, Dimitri Komatitsch†, Bor-Shouh Huang, and Jeroen Tromp

Abstract We use the spectral-element method to simulate strong ground motion throughout the Taipei metropolitan area. Mesh generation for the Taipei basin poses two main challenges: (1) the basin is surrounded by steep mountains, and (2) the city is located on top of a shallow, low-wave-speed sedimentary basin. To accommodate the steep and rapidly varying topography, we introduce a thin high-resolution mesh layer near the surface. The mesh for the shallow sedimentary basin is adjusted to honor its complex geometry and sharp lateral wave-speed contrasts. Variations in Moho thickness beneath Northern Taiwan are also incorporated in the mesh. Spectral-element simulations show that ground motion in the Taipei metropolitan region is strongly affected by the geometry of the basin and the surrounding mountains. The amplification of ground motion is mainly controlled by basin depth and shallow shear-wave speeds, although surface topography also serves to amplify and prolong seismic shaking.

Introduction

Taipei City in Taiwan is one of the most densely populated metropolitan areas situated on top of a shallow sedimentary basin. Over the past 20 yr, seismic disasters in the Taipei metropolitan area, particularly the 21 September 1999 Chi-Chi (M_w 7.6) and 31 March 2002 east coast (M_L 6.8) earthquakes, have caused significant damage with considerable casualties (e.g., Wen *et al.*, 1995; Wen and Peng, 1998; Chen, 2003). Furthermore, recent studies suggest that moderate earthquakes near the basin also have the potential to cause strong ground shaking throughout the city (Lin, 2005).

Compared to the Los Angeles basin, the Taipei basin is small, about 20×20 km at the surface, and relatively shallow, with a maximum depth of less than 1000 m. It is surrounded by varied topography, including mountains, tableland, and a volcano group (Fig. 1a), collectively producing changes in elevation varying between sea level and about 1120 m. There are two major discontinuities in the basin: the SongShan formation and the basin basement (Fig. 1b). The SongShan formation is a shallow, low-shear-wave-speed sedimentary layer. The basin is surrounded by

Tertiary basement with a deepest extent of about 700–1000 m (Wang *et al.*, 2004). Taipei city's high-rise buildings, including the world's current tallest building Taipei 101 in the eastern part of the basin, make the heavily populated region particularly vulnerable to earthquakes.

In recent years, numerical simulations have been successfully used to study the complex nature of strong ground motion due to earthquakes (see, e.g., Olsen *et al.*, 1995, 1996; Wald and Graves 1998; Komatitsch *et al.*, 2004) and the related seismic hazard (e.g., Olsen, 2000). However, for the Taipei basin, slow, laterally variable sedimentary layers and sharp transitions between shallow sediments and the underlying basement pose a considerable numerical challenge. Furthermore, the notable topography around Taipei city makes the issue even more daunting. Lee, Huang, *et al.* (2006) used a finite-difference method to assess strong ground motions in the Taipei area for a variety of basin models. However, due to the difficulty of incorporating the free surface condition in the finite-difference method (see for instance Robertsson, 1996), surface topography was not considered in their analysis.

To accommodate the considerable surface topography as well as the highly variable low-wave-speed sedimentary basin, we will use the spectral-element method (SEM) to simulate seismic-wave propagation in the Taipei metropolitan area. The SEM is a numerical technique developed more than

*Present address: Institute of Geophysics and Planetary Physics, Scripps Institution of Oceanography, University of California, San Diego, California 92093-0225

†Also at: Institut Universitaire de France, 103 Boulevard Saint-Michel, 75005 Paris, France.

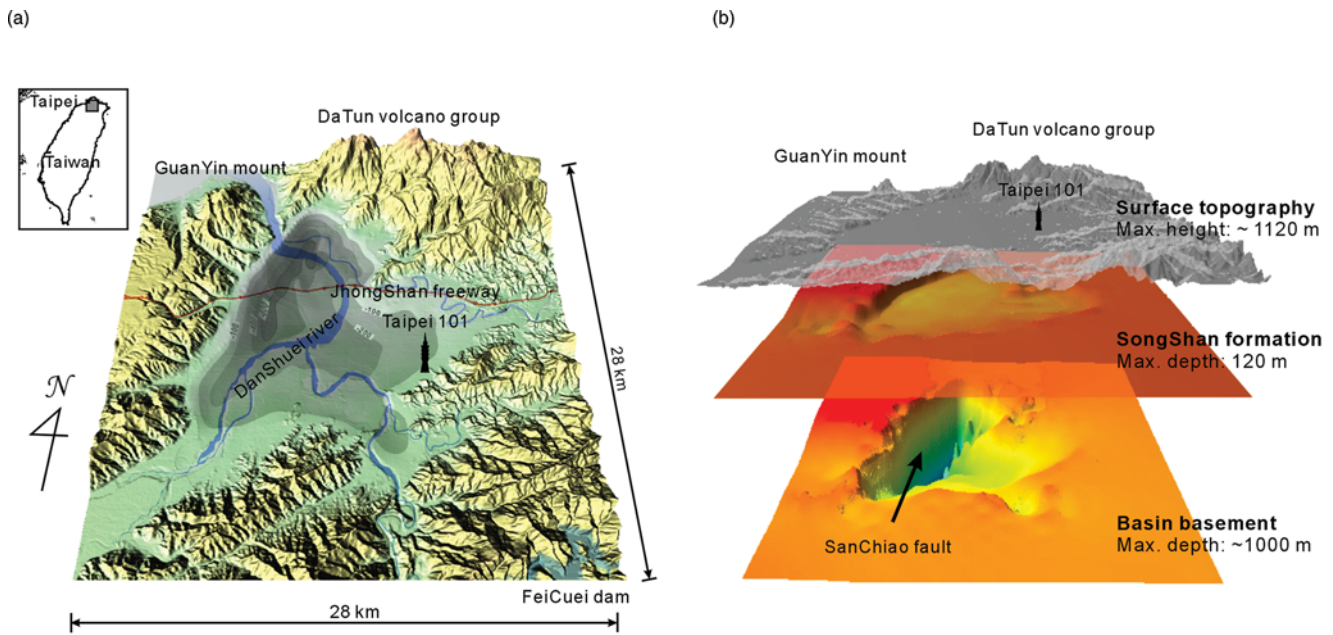


Figure 1. (a) Map view of the Taipei basin. The depth of the basement is represented by gray colors. The red line shows the ZhongShan freeway across the basin. The location of the world's current tallest building, Taipei 101, is indicated in the eastern part of the basin. (b) Perspective view of the two major discontinuities in the Taipei basin: The SongShan formation and the basin basement. Surface topography around the basin is shown at the top of the figure.

20 yr ago to address problems in computational fluid dynamics (Patera, 1984). It is based upon a weak formulation of the equations of motion and naturally incorporates topography. Komatitsch and Vilotte (1998) and Komatitsch and Tromp (1999) provide a detailed introduction to the SEM for 3D seismic-wave propagation. The method has been subsequently applied in many areas of seismology (e.g., Komatitsch *et al.*, 2002; Chaljub *et al.*, 2003; Komatitsch *et al.*, 2004). The biggest challenge for the successful application of the SEM lies in the design of the mesh (e.g., Komatitsch *et al.*, 2005). In this study, we present a new mesh implementation to improve mesh quality and related numerical stability. Based upon this implementation, realistic topography and complex subsurface structures can be efficiently incorporated within the SEM mesh. We assess the quality of our Taipei basin model and the related mesh by simulating a moderate earthquake, which occurred near the basin on 23 October 2004. The effects of basin structure, the influence of realistic surface topography, and their combined interaction are investigated in this article.

Taipei Basin Model and Mesh Implementation

Model Setting

Figure 2 shows the Taipei basin mesh we constructed. The size of the region is 101.9×87.5 km horizontally and from $+2.89$ to -100 km vertically. This model covers most of northern Taiwan because we wish to take account of possible earthquakes and/or seismic damage outside of the

basin. We have incorporated most of currently available relevant seismological information in the model, including surface topography, basin geometry, Moho topography, and 3D wave-speed heterogeneity. The 3D basin geometry and the related wave-speed model are derived from Wang *et al.* (2004), in which seismic reflection data and borehole logs

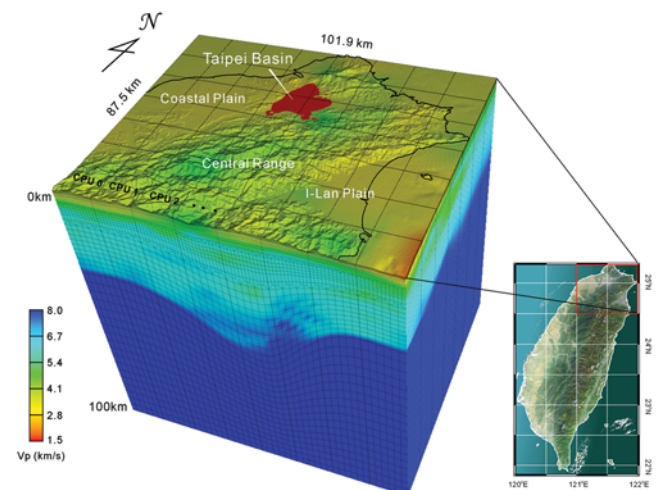


Figure 2. Spectral-element mesh for northern Taiwan. The size of the model is 101.9×87.5 km horizontally and from $+2.89$ to -100 km vertically. The three-dimensional P -wave-speed variations are represented by the rainbow color scale. The Taipei basin is located in the middle part of the model, and is characterized by relatively low wave speeds compared to surrounding areas.

are combined to characterize the Tertiary basement, the Quaternary layers above the basement, and their compressional- and shear-wave speeds. The slowest compressional- and shear-wave speeds in the basin model are 1.5 and 0.2 km/sec, respectively. We embed the basin model in a regional tomographic model derived by Kim *et al.* (2005). The nominal resolution of this background tomographic model is 8 km horizontally and 2 km vertically. The shear-wave-speed outside the basin is computed from the compressional wave-speed model based upon the assumption of a value of 0.25 for Poisson's ratio. The location of the Moho is determined by the 7.8 km/sec isovelocity surface in the regional tomographic model. We assign constant wave speeds beneath the Moho ($V_P = 8.0$ km/sec and $V_S = 4.6$ km/sec) to represent the upper mantle. Throughout the entire model, density is defined based upon the empirical rule $\rho = V_P/3 + 1280$ (McCulloh, 1960; Stidham *et al.*, 2001) and is constrained to lie between 2000 and 3000 kg m⁻³. Hauksson *et al.* (1987) determined a shear quality factor of 90 for the Los Angeles basin. Because of a lack of better attenuation information, we adopt the same shear quality factor for the Taipei basin and a Q of 500 elsewhere (i.e., relatively strong attenuation in the sediments and weak attenuation in the bedrock).

Realistic Topography

We incorporate surface topography based on digital elevation model (DEM) data generated using paired aerial photographs taken nearly two decades ago by the Agricultural and Forestry Aerial Survey Institute in Taiwan, which provide a resolution of 40 m for all of Taiwan. As shown in Figure 2, surface topography is honored by the SEM mesh. To incorporate high-resolution topography at the top of the model, we use mesh doubling as a function of depth (e.g., Komatitsch and Tromp, 1999) to accommodate a finer mesh near the surface (Fig. 3). Three consecutive mesh doublings facilitate an increase in element size with depth in accordance with corresponding increases in wave speeds (Fig. 3a). Five control surfaces are used at various depths. The top of the model is controlled by the DEM surface topography. Right below the surface we introduce a buffer layer—a smoothed version of the surface topography—which is used to dampen mesh distortions induced by the DEM topography. The buffer layer is critical to ensure the accurate and stable accommodation of realistic surface undulations. This layer also defines the top of the first mesh doubling. The top of the second doubling is defined by 93% of the distance from the Moho to the buffer layer, and the third doubling is defined by 75% of this distance. The deepest control surface is the Moho, which follows the 7.8 km/sec isovelocity surface. A close-up view of the shallow mesh is shown in Figure 3b to illustrate how the buffer layer is implemented.

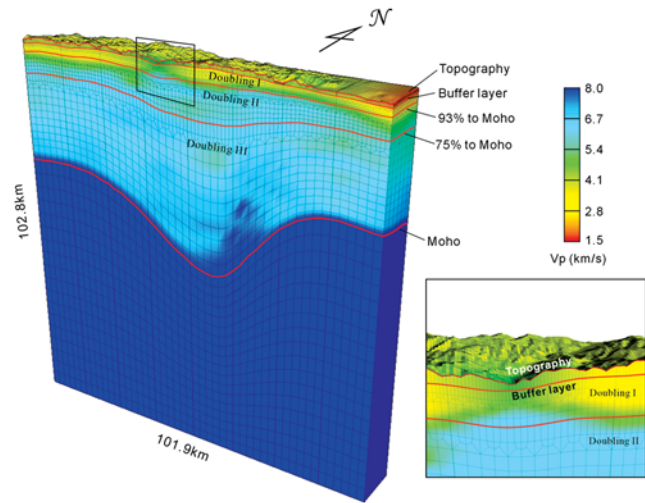


Figure 3. Cross-sectional view from the south of the northern Taiwan spectral-element mesh (left). A buffer layer is introduced to dampen mesh distortions due to steep surface topography, as emphasized in the close-up view (right). The size of the mesh elements is doubled three times to reduce the numerical cost of the simulations by reducing the number of spectral elements and to allow for a larger time step in the explicit conditionally stable time scheme. The first doubling starts right below the bottom of the buffer layer, the second doubling starts at 93% of the distance from the Moho to the buffer layer, and the third doubling starts at 75% of this distance.

Meshing the Sedimentary Basin

The shallow sedimentary basin underneath Taipei city is introduced between the surface topography and the buffer layer (Fig. 4). Seismic-wave speed in the basin is quite low, as illustrated by the sharp contrast between the basin and the surrounding basement in Figure 4. Compared to the Los Angeles basin, the Taipei basin is relatively small and shallow. If we use the same meshing strategy as that of Komatitsch *et al.* (2004) for the Los Angeles basin to mesh the Taipei basin, the basement layer can only honor a small portion of the deepest part of the basin, as illustrated in Figure 4a. Based upon this implementation, most of the basin boundaries are not constrained by the mesh. Furthermore, the deep basin has lower resolution due to the stretching of the mesh between the surface and the basement (Fig. 4a). To overcome these limitations, we adjust the spectral elements within the sedimentary basin to redefine the basin boundary mesh (Fig. 4b). Several empirical criteria are used to define how and where to move the affected elements. A minimum distance (ΔD_b) is assigned to constrain the smallest allowable distance of a mesh node from the basin boundary (see the close up of the basin basement mesh in Fig. 4b). The smaller the grid spacing, the smaller the timestep needs to be to ensure numerical stability, because the SEM is based on an explicit conditionally stable finite-difference time integration scheme (e.g., Komatitsch and Vilotte, 1998; Komatitsch and Tromp, 1999). Thus, ΔD_b

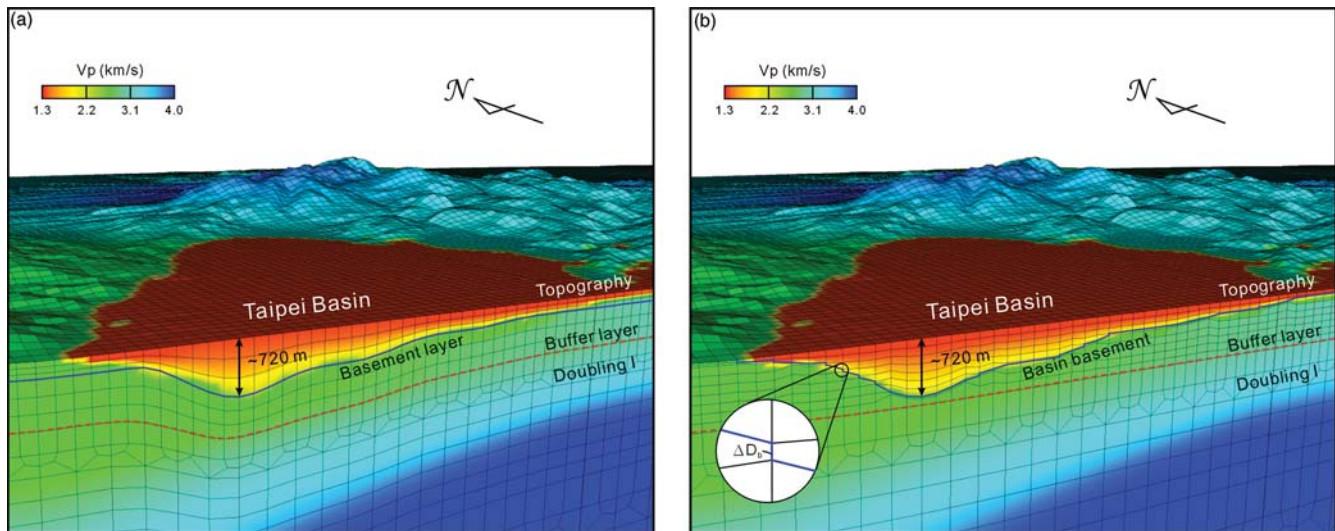


Figure 4. Two different mesh implementations for the Taipei basin. (a) Mesh implementation similar to the Los Angeles basin SEM mesh developed by Komatitsch *et al.* (2004). Note that only the lower parts of the basin are honored by the mesh, and that there are relatively few elements between the surface and the basement in the deeper parts of the basin. (b) New mesh implementation for the Taipei basin SEM mesh. The two major control layers, the buffer layer and the basement layer, are indicated by the blue and red lines, respectively. A close-up shows the relation between the minimum distance ΔD_b and the basin basement mesh.

needs to be carefully ascertained to obtain the optimal trade-off between numerical efficiency and model accuracy. By adjusting the location of the mesh nodes based upon these criteria, we obtained a mesh that honors the complex basin boundary.

To demonstrate the stability of the basin mesh shown in Figure 4b, we consider a 3D basin model ($V_P = 3.0$ km/sec; $V_S = 1.155$ km/sec) over a half-space ($V_P = 6.0$ km/sec; $V_S = 3.464$ km/sec) with a strike-slip point source and two vertical receiver arrays, as illustrated in Figure 5. Three different mesh implementations for this basin model are considered: model a shows a simple mesh with no sophisticated buffering, similar to that originally implemented for the Los Angeles basin by Komatitsch *et al.* (2004) (Fig. 5a); model b shows an irregular, distorted mesh which honors the Taipei basin geometry (Fig. 5b); and model c shows a regular mesh with a fourfold increase in mesh density in the vertical direction in the shallow part of the model (Fig. 5c). The mesh implementation (model c) provides the highest accuracy for both the model and the synthetic waveforms in the test, at the cost of a significant increase in the computational burden. Two vertical receiver arrays record the wave field, one at the basin center (receivers I) and the other at the deepest part of the basin (receivers II), which cut across the basement at depths of 206 and 711 m, respectively. A strike-slip point source (strike, 0° ; dip, 90° ; and rake, 0°) with a depth of 2 km and a Gaussian source time function with a half-duration of 0.15 sec is located outside the eastern part of the basin. All the synthetic waveforms are low-pass filtered with a corner frequency of 3 Hz. The results for the three components of velocity are shown in the right panels in Figure 5. The syn-

thetic waveforms obtained based upon mesh implementation (model a) do not fit the reference waveforms derived based upon the high-resolution mesh (model c). This is obvious from the close-up views for shorter time windows. The synthetic waveforms derived based upon the mesh implementations (models b and c) are indistinguishable at both sets of receivers, even for receivers located close to the basement, where the basin mesh is adjusted and distorted.

From these experiments we conclude that the Taipei basin mesh implementation (model b) is stable, accurate, and computationally efficient. Based upon this approach, the complex basin boundary can be precisely defined in both the deep and the shallow parts. For future studies, we are actively developing strategies for the generation of general, unstructured hexahedral meshes for complex models (Casarotti *et al.*, 2006) based upon the CUBIT geometry and mesh generation toolkit (Sandia National Laboratories, <http://cubit.sandia.gov>).

Simulation of the 23 October 2004 Taipei Earthquake (M_L 3.8)

There are several active faults that pose potential seismic hazards for the Taipei metropolitan area. However, there is relatively little seismic activity near the Taipei basin, and most earthquakes are too small to be recorded by the strong-motion array that is installed in the basin. On 23 October 2004, a small earthquake (M_L 3.8) occurred near the southeastern edge of the basin at a depth of 9.2 km and was reported by the Central Weather Bureau (CWB) of Taiwan. The fault plane solution derived from a 3D moment-tensor inversion indicates a normal fault striking 195° , dipping

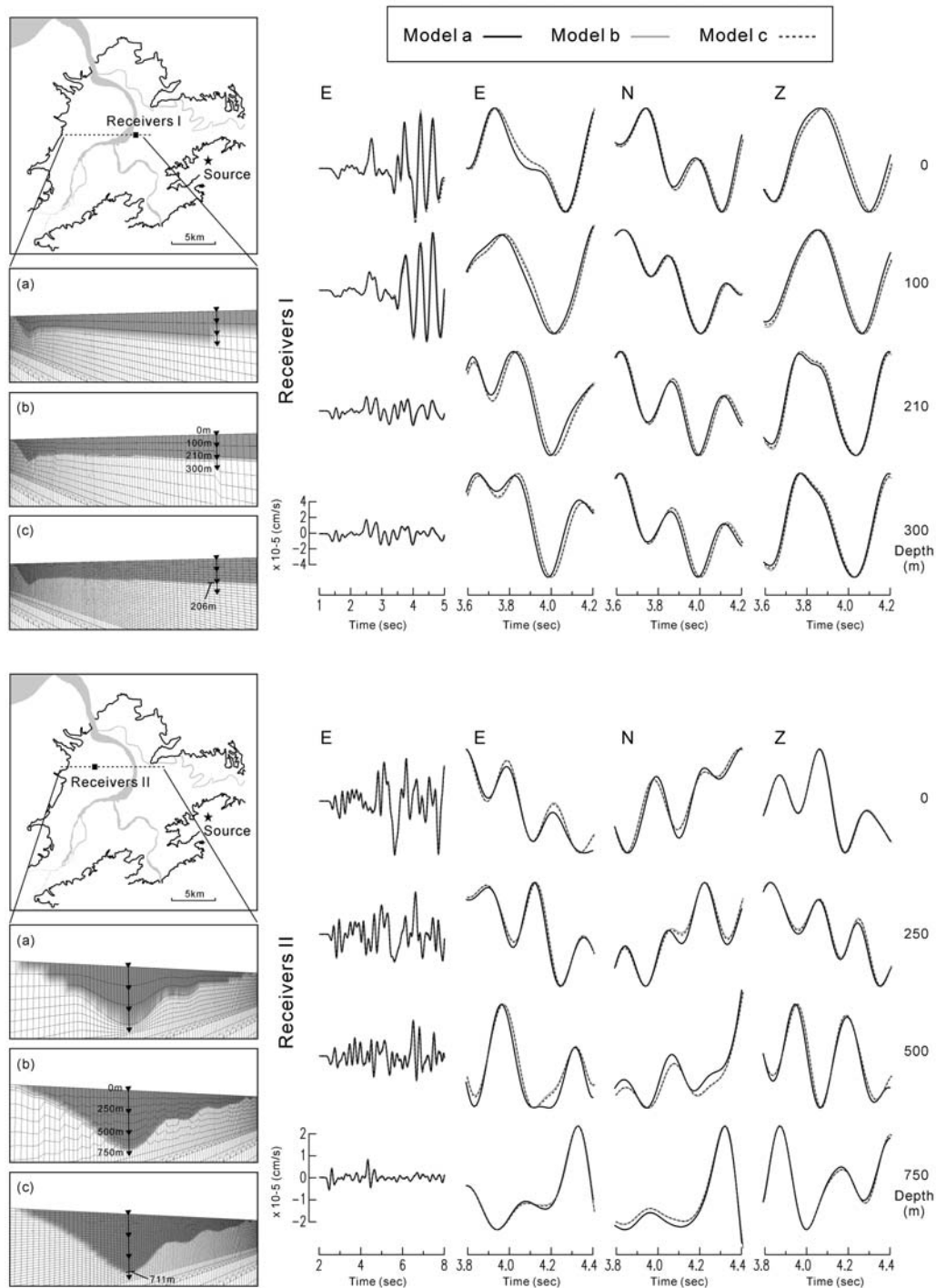


Figure 5. Stability tests for three different mesh implementations for the Taipei basin without topography but with the sedimentary basin. (a) Simple mesh implementation without sophisticated buffering similar to that used by Komatitsch *et al.* (2004) for the Los Angeles basin. (b) New mesh implementation used in this study. (c) Regular mesh without distortions induced by the basin but with a four-fold increase in mesh density in the vertical direction. The models consist of a 3D basin ($V_P = 3.0$ km/sec, $V_S = 1.155$ km/sec, $\rho = 2.3$ g/cm³) over a homogeneous half-space ($V_P = 6.0$ km/sec, $V_S = 3.464$ km/sec, $\rho = 2.7$ g/cm³). The earthquake source is a strike-slip point source (epi-center 121.58° E, 25.02° N, depth 2.0 km). Two vertical receiver arrays are used to record the wave field, one located at the basin center (receivers I), and the other at the deepest part of the basin (receivers II). The three-component synthetic velocity waveforms computed for models (a), (b), and (c) are low-pass filtered with a corner frequency of 3 Hz, and are represented by the solid, gray, and dotted lines, respectively, in the right-hand panels.

49°, and raking 140° (Lee, Huang, *et al.*, 2006). Because the earthquake is small, the details of the source process can be ignored, and we can use a simple point source instead. This event gives us an excellent opportunity to assess our current velocity model and the Taipei basin SEM mesh. Because the epicenter of the earthquake is close to the basin, we focus on the Taipei metropolitan area, where most strong-motion instruments were triggered.

We use the SPECSEM3D software package developed by Komatitsch *et al.* (2004) and decompose the study area into 324 mesh slices (i.e., 324 processors) for parallel computing based upon the message-passing interface (MPI) (Gropp *et al.*, 1996). In each spectral element we use a polynomial degree of $N = 4$, and thus each element contains $(N + 1)^3 = 125$ Gauss–Lobatto–Legendre integration points. The average distance between Gauss–Lobatto–Legendre integration points at the surface is 28 m, that is, sufficiently small to resolve the DEM data, and the slowest shear waves within the basin for simulations are accurate up to 1.0 Hz. The simulations are carried out on Caltech’s CITerra Dell cluster (512 dual-processor quad-core nodes). The total number of spectral elements and Gauss–Lobatto–Legendre points in the model is 4,500,000 and 297,000,000, respectively. These simulations require 116 gigabytes of memory and the average wall-clock time is 9.5 hr.

Snapshots of the simulation for the east, north, and vertical components of the velocity wave field (low-pass filtered with a corner frequency of 1.0 Hz) are displayed in Figures 6c, respectively. The *P* wave reaches the surface with a relatively weak amplitude at approximately 3 sec. After 6 sec, the slower but stronger *S* wave reaches the surface and propagates through the basin with significant amplification. The wavefronts slow down and are dramatically distorted due to the low shear-wave speeds in the basin, especially within the soft sedimentary layer. Short-period surface waves propagating after the *S* wave are observed from 6 to 9 sec. These surface waves are generated by reflections and mode conversions at the free surface and at the shallow basin edges. Yalcinkaya and Alptekin (2005) illustrate similar contributions of basin-edge-induced surface waves to site amplifications. Energy is trapped and reflected within the low-wave-speed sediments. This effect is particularly clear in the eastern part of the basin, where the basement is close to the ground surface and has a large wave-speed contrast relative to the hard rock. After 12 sec, the main body-wave phases have propagated out of the basin; however, the basin continues to shake for several seconds. This longer shaking comes from two different sources: trapped and reflected waves from the basin boundary as described earlier, and reflected and refracted waves generated by scattering from the surrounding mountains. As a result of the source radiation pattern, the horizontal components usually have larger amplitudes than the vertical component (Fig. 6).

Comparisons between observed velocity records from the Central Weather Bureau strong-motion array (TSMIP) and the corresponding synthetic seismograms are shown

in Figure 7. Most of the triggered stations are located near the epicenter, in the middle part of the basin, and along the basin edge. Records from stations located in the western part of the basin have poorer quality, and therefore it is difficult to distinguish the signal from the background noise. We focus on stations with a good record quality, which are mostly located in the eastern part of the basin, close to the epicenter. There are several prominent phases after the initial body waves, especially on the vertical component. For a moderate regional earthquake at epicentral distances smaller than 15 km, these records are quite complex. Compared to the observations in Figure 7, the synthetics explain the major characteristics of the observed records. The synthetics for the horizontal (north and east) components explain both the major phases and the later arrivals quite well. On the smaller-amplitude vertical component, however, there are larger discrepancies. In some cases the background noise dominates the data and increases waveform complexity. Some synthetics cannot explain the data on all three components, such as at stations TAP005 and TAP032. This may be due to inaccuracies in the basin model, such as the lack of a 3D attenuation model, 3D velocity structure in the deeper parts of the basin, and insufficient resolution of lateral wave-speed variations and basin geometry.

We analyze the maximum particle acceleration within the records to obtain the information on peak ground acceleration (PGA) distribution (Fig. 8). The observed PGA values are obtained from the norm of all three components (low-pass filtered with a corner frequency of 1.0 Hz) to compare with the corresponding simulated results. Significant amplification is observed in the basin, with relatively large PGA values compared to its surroundings. However, large PGA values are controlled both by the basin geometry and by the source radiation pattern. The trade-off between source and site effects in the near field is discussed in S. J. Lee *et al.* (unpublished manuscript, 2006). Because the epicenter is located close to the basin, source radiation dominates the PGA distribution in the near-field records. Combined source radiation and basin amplification effects produce large PGA values in the southeastern part of the basin. The northern part of the basin exhibits relatively small observed and simulated PGA values. Stations with small PGA values are sometimes located surprisingly close to stations with relatively large PGA values, indicating that there must be sharp lateral variations in material properties, probably associated with the shallow geotechnical layer, which is out of the frequency range used in the simulation. Outside the basin the PGA values shown in Figure 8 exhibit a symmetric pattern centered on the epicenter with a strike determined by the focal mechanism. Note, however, that some anomalously high PGA values are predicted to be associated with mountain ridges and peaks. Because of a lack of station coverage in the mountains, we cannot confirm these predictions with corresponding observations.

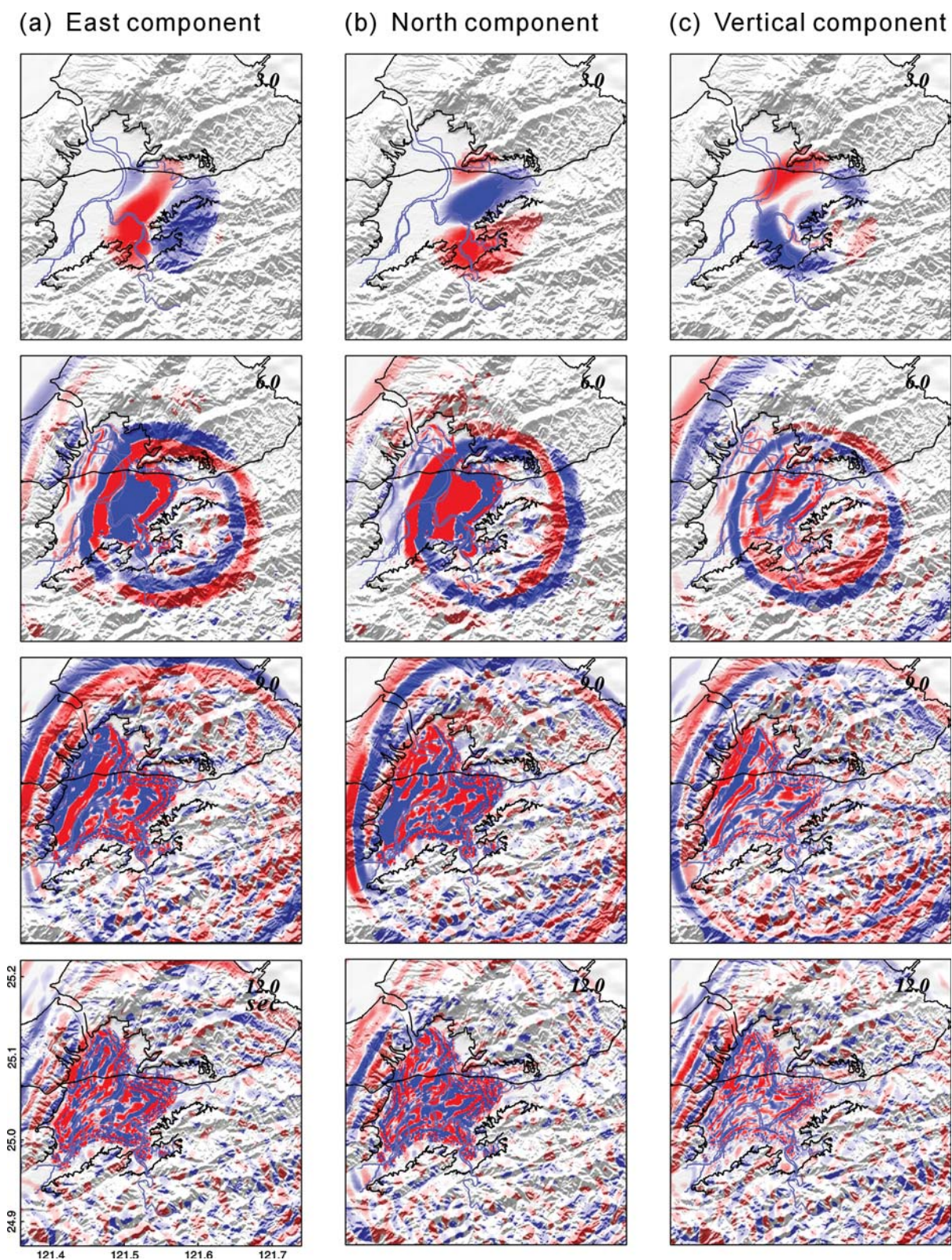


Figure 6. Snapshots of a simulation of the 23 October 2004 M_L 3.8 Taipei earthquake whose epicenter is indicated by the star. (a) East component. (b) North component. (c) Vertical component. Red colors indicate positive velocities and blue colors indicate negative velocities. The wavefronts are distorted and amplified in the basin, especially on the horizontal components.

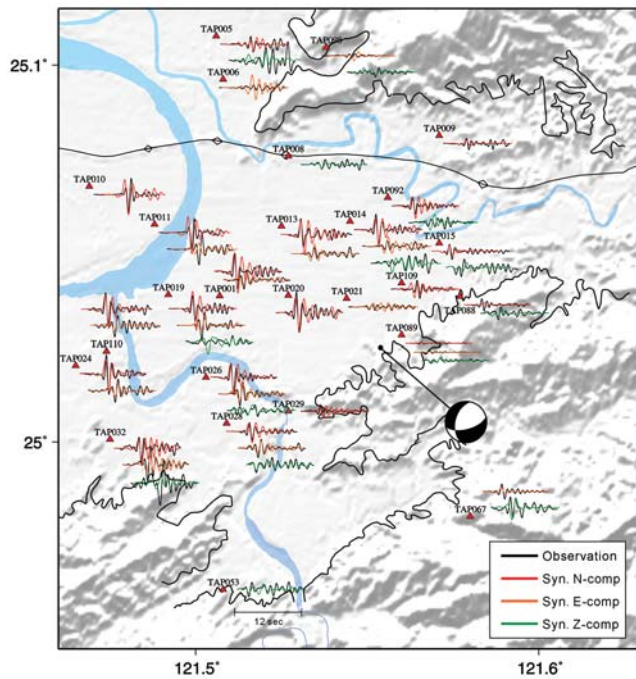


Figure 7. Comparison between synthetic waveforms and strong-motion records of the 23 October 2004 M_L 3.8 Taipei earthquake, whose mechanism is represented by the beach ball. The velocity waveforms are band-pass filtered between 0.1 and 1.0 Hz. Recorded data are represented by black lines and synthetics are represented by red (north component), orange (east component), and green (vertical component) lines.

Discussion

Although the results of the simulation are still insufficiently accurate to allow for a wiggle-for-wiggle comparison between data and synthetics, we are beginning to unravel the competing amplification effects associated with the basin, the source radiation pattern, and surface topography. Based upon the mesh implementation developed in this study, the 40×40 m DEM data can be accommodated without additional smoothing or severe mesh distortions. This gives us an opportunity to investigate the effects of topography on the seismic-wave field in detail. To this end, we considered three different models: (1) a 3D velocity model without topography, (2) a 3D velocity model with surface topography but without a sedimentary basin, and (3) a 3D velocity model with both a sedimentary basin and surface topography. As before, the 3D velocity model is that of Kim *et al.* (2005) and the basin model is from Wang *et al.* (2004).

To assess the effects of topography, we consider the 23 October 2004 Taipei earthquake by using a point source with a half-duration of 0.5 sec. Figure 9b illustrates the differences between simulations based upon a 3D velocity model with and without topography. It is obvious that topography can produce complex wave propagation behavior, with seismic energy reflected and scattered by the mountains, especially in the eastern part of the basin. One can observe a

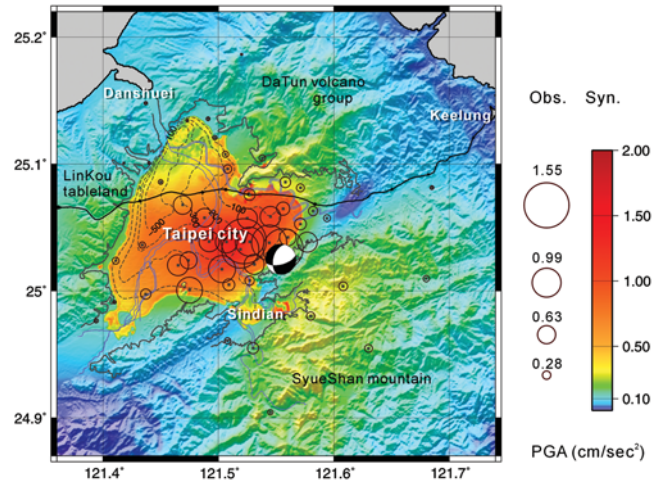


Figure 8. Comparison between simulated and observed peak ground acceleration (PGA). The observed PGA values are obtained from the norm of all three components (low-pass filtered with a corner frequency of 1.0 Hz) to compare with the corresponding simulated results. The observed PGA is shown by the open circles, and the simulated results are drawn using the rainbow scale shown to the right. The epicenter and source mechanism of the Taipei earthquake are represented by the beach ball.

major reflection coming from a southeasterly direction, following the trend of mountains that borders the basin to the east. Note that compressional (P) waves (around 3 sec) are not significantly affected by topography, but that shear (S) waves (around 6 sec) produce obvious reflections. Additional mountain-reflected waves can be identified after approximately 9 sec. These reflected waves propagate back into the basin, thus producing longer shaking in the city of Taipei.

The PGA amplification factor is obtained by subtracting the PGA value for the model without topography (Fig. 9a) from the value for the model with topography (Fig. 9b), dividing the result by the PGA value for the model without topography, and multiplying it by 100 to obtain a percentage. Figure 10 illustrates that surface topography increases the PGA at mountain tops and ridges, whereas valleys usually have a reduced PGA, that is, a negative PGA amplification factor. Examples of synthetic waveform comparisons are shown in the right panels of Figure 10. The P waveforms are almost identical in both models, while the amplitudes and travel times of the S waves differ noticeably, and there is a significantly longer duration of shaking in the simulation for the model with topography. PGA amplification values vary generally by $\pm 50\%$, and the difference in PGA amplification between a valley and a ridge can be as high as a factor of 2.

The effects of basin geometry and low-wave-speed sediments on strong ground motion can easily be observed in snapshots of the simulated wave field (Fig. 9). Snapshots for a model with both a basin and topography (Fig. 9c) illustrate that ground shaking within the basin is relatively strong and very complex. When the waves travel in the basin,

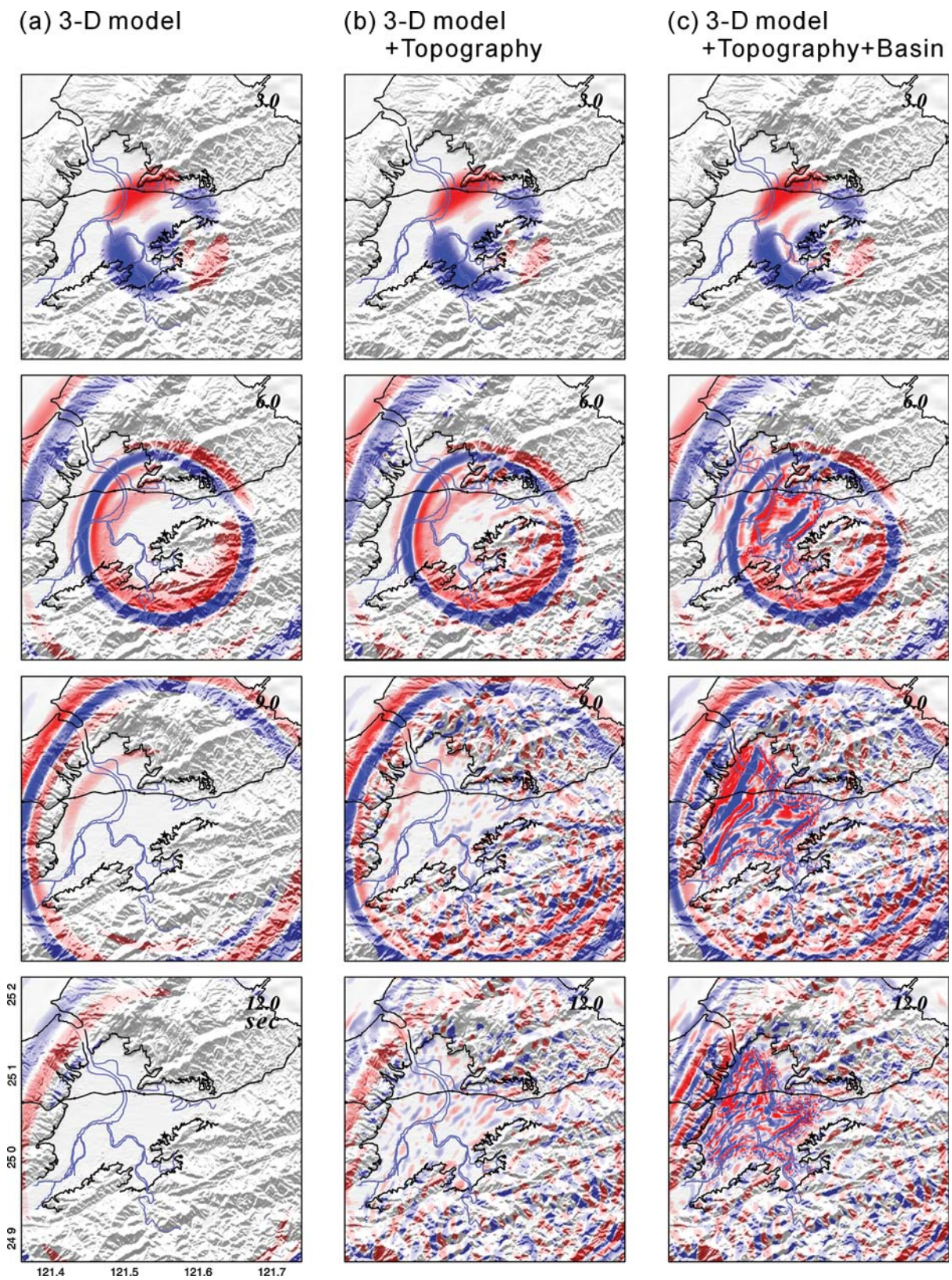


Figure 9. Snapshots obtained based on three models: (a) 3D velocity model with a flat ground surface. (b) 3D velocity model with surface topography. (c) 3D velocity model with basin and surface topography. The vertical component velocity wave fields are displayed. Red colors indicate positive velocities and blue colors indicate negative values. The epicenter of the Taipei earthquake is represented by the star.

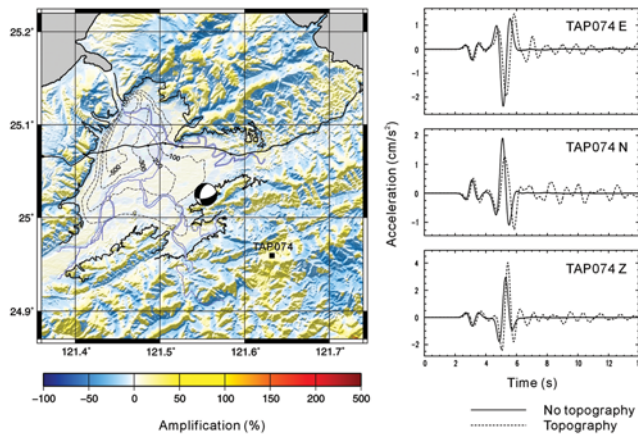


Figure 10. PGA amplification factor due to surface topography. The PGA amplification factor is obtained by subtracting the PGA value for the model without topography from the value for the model with topography, dividing the result by the PGA value for the model without topography, and multiplying the result by 100 to obtain a percentage. The panels to the right show an example of synthetic waveforms at station TAP074 for the models with and without topography (from top to bottom, the east, north, and vertical components).

short-period surface waves (Rayleigh waves), which propagate after the S wave, are clearly observed (6 sec). These surface waves are generated by reflections and mode conversions between the basement and the free surface. The duration of shaking is increased relative to the flat model shown in Figure 9a, because waves are trapped and reflected within the low-wave-speed sediments. Furthermore, complex reflections caused by the topography that surrounds the basin further increases the duration of shaking (after 9 sec).

The influence of the basin is very clear from an analysis of the PGA amplification factor (Fig. 11). Compared to the amplification factor in mountainous areas (which is about $\pm 50\%$), the sediments in the basin amplify the shaking by more than 100%. Some areas within the basin have particularly anomalous amplification values, for example, the southeastern part of the basin (labeled area I in Fig. 11) and the northern part of the basin (area II). Note that the amplification values in these areas can be more than five times larger than those shown in Figure 9a. PGA amplification in the mountains is almost the same as in Figure 10. However, there is an exception on the western side of the basin (area III in Fig. 11), where the amplification values decrease dramatically. This phenomenon is due to the fact that most of the energy radiated in this direction is deflected by the basin, thereby reducing the PGA values in the shadow of the basin. Examples of synthetic waveforms from a station located in the basin are shown in the right panels of Figure 11. The peak values of ground acceleration increase dramatically, especially on the horizontal components. Compared to the result for the model without a basin, the major phases have longer travel times due to the low wave speeds in the basin. Strong

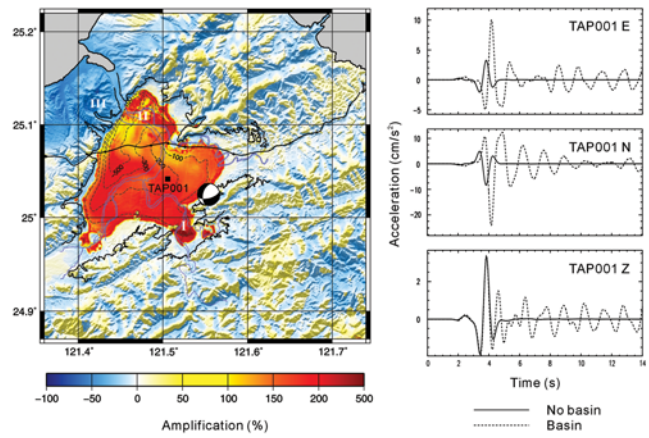


Figure 11. PGA amplification factor due to the basin and surface topography. An example of synthetic waveforms recorded at station TAP001 located within the basin is shown in the right panels (from top to bottom the east, north, and vertical components). Areas I, II, and III denote locations with anomalous amplification values. Note that in some areas the Taipei basin can amplify the PGA value by a factor of up to 5.

later phases can be observed for more than 10 sec in the synthetic waveforms as a result of a combination of basin reflections and mountain refractions.

The quality factor Q is an important parameter in the modeling of seismic-wave propagation in the Taipei basin. Because of the lack of a reference Taipei basin attenuation study we adopt the shear quality factor, Q_μ , of 90 determined by Hauksson *et al.* (1987) for the Los Angeles basin. To investigate the effects of the choice of shear Q on the simulations, we compare the results between different shear quality factors in Figure 12. The effects of topography with and without Q_μ in the bedrock are also shown. Our results indicate that the amplitudes of waveforms both in the basin (TAP001) and in a mountainous area (TAP074) are reduced compared to the results without attenuation, especially for the peak amplitude (S) wave. However, shear attenuation has less influence on topographic scattering, and this means that topographic scattering is more pronounced in the time series when attenuation is incorporated in the bedrock. For varying shear Q values in the basin, our results show that the simulated waveforms are insensitive to perturbations in shear Q . This might be due to the short distance to the hypocenter, as well as the fact that the basin is relatively small and shallow.

Conclusions

We developed a new spectral-element mesh implementation to accommodate topography and a complex basin geometry for the Taipei metropolitan area in northern Taiwan. A thin buffer layer was used to produce a fine mesh near the surface, and steep topography obtained from digital elevation data was incorporated without additional smoothing. We demonstrated that topography can change PGA values

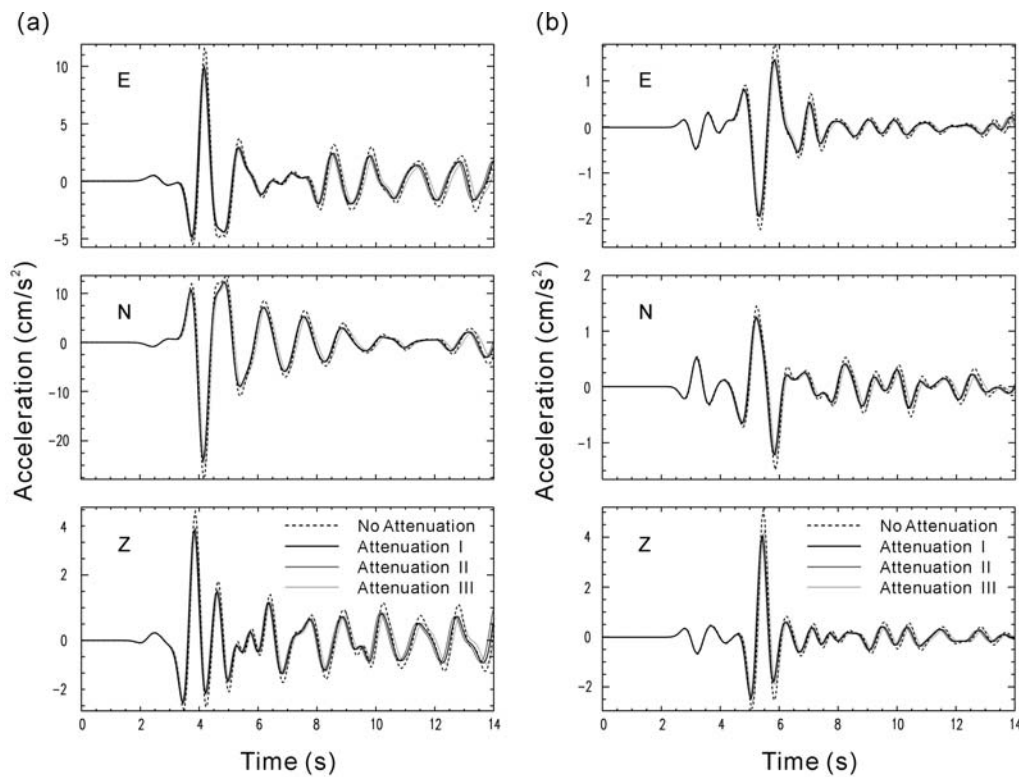


Figure 12. Effect of the shear quality factor Q_μ on simulations of the Taipei earthquake recorded (a) inside the Taipei basin (TAP001) and (b) in mountainous areas (TAP074). All three components are filtered between 0.1 and 1.0 Hz. Dashed lines show the result without attenuation. The shear Q is set to 500 in the bedrock when attenuation is included. In the basin, we consider three shear Q values: (I) $Q_\mu = 90$, (II) $Q_\mu = 150$, and (III) $Q_\mu = 50$. The associated synthetic waveforms are represented by solid lines with various colors as indicated in the lower legend.

in mountainous areas by $\pm 50\%$ compared to the response of a half-space. To accommodate the small, low-wave-speed sedimentary basin, we systematically adjusted the mesh in the vicinity of the basin edges. The meshing technique developed in this study can probably be used to construct a spectral-element mesh of all of Taiwan or elsewhere in future studies. By considering both the low-wave-speed sediments in the Taipei basin and the surrounding mountains, our results indicate that the Taipei basin can amplify ground motion by a factor of up to 5 compared to a model without a basin and topography. Furthermore, the basin and surrounding mountains significantly increase the duration of shaking in the Taipei metropolitan area.

Acknowledgments

This research is a collaborative effort between California Institute of Technology, Institute of Earth Sciences, Academia Sinica (IESAS) (Taiwan), and National Central University (NCU) (Taiwan). The authors would like to thank S.-B. Yu and J.-P. Avouac for making this collaboration possible. Special thanks go to IESAS and the Caltech Seismo Lab, where many fruitful discussions occurred. Most of the simulations were carried out on Caltech's Division of Geological & Planetary Sciences Dell cluster. This research was supported by Academia Sinica, Taiwan, Republic of China, under Grant Number AS-94-TP-A08, and by the U.S. National Science Foundation under Grant Number EAR-0309576.

References

- Casarotti, E., S. J. Lee, D. Komatitsch, A. Piersanti, and J. Tromp (2006). CUBIT and seismic-wave propagation based upon the spectral-element method: an advanced unstructured mesher for complex 3D geological media (Abstract S51E-06), *EOS* **87**, no. 52, (Fall Meet. Suppl.), S51E-06.
- Chaljub, E., Y. Capdeville, and J. P. Vilotte (2003). Solving elastodynamics in a fluid-solid heterogeneous sphere: a parallel spectral element approximation on non-conforming grids, *J. Comp. Phys.* **187**, no. 2, 457–491.
- Chen, K. C. (2003). Strong ground motion and damage in the Taipei basin from the Moho reflected seismic-waves during the March 31, 2002, Hualien, Taiwan earthquake, *Geophys. Res. Lett.* **30**, 1151–1154.
- Gropp, W., E. Lusk, N. Doss, and A. Skjellum (1996). A high-performance, portable implementation of the MPI message passing interface standard, *Parallel Comput.* **22**, 789–828.
- Hauksson, E., T. L. Teng, and T. L. Henyey (1987). Results from a 1500 m deep, three-level downhole seismometer array: site response, low Q values, and f_{max} , *Bull. Seismol. Soc. Am.* **77**, 1883–1904.
- Kim, K. H., J. M. Chiu, J. Pujol, K. C. Chen, B. S. Huang, Y. H. Yeh, and P. Shen (2005). Three-dimensional V_p and V_s structural models associated with the active subduction and collision tectonics in the Taiwan region, *Geophys. J. Int.* **162**, 204–220.
- Komatitsch, D., and J. Tromp (1999). Introduction to the spectral-element method for 3-D seismic-wave propagation, *Geophys. J. Int.* **139**, 806–822.
- Komatitsch, D., and J. P. Vilotte (1998). The spectral-element method: an efficient tool to simulate the seismic response of 2D and 3D geological structures, *Bull. Seismol. Soc. Am.* **88**, no. 2, 368–392.

- Komatitsch, D., Q. Liu, J. Tromp, P. Süß, C. Stidham, and J. H. Shaw (2004). Simulations of ground motion in the Los Angeles basin based upon the spectral-element method, *Bull. Seismol. Soc. Am.* **94**, 187–206.
- Komatitsch, D., J. Ritsema, and J. Tromp (2002). The spectral-element method, Beowulf computing and global seismology, *Science* **298**, 1737–1742.
- Komatitsch, D., S. Tsuboi, and J. Tromp (2005). The spectral-element method in seismology, in *Seismic Earth: Array Analysis of Broadband Seismograms*, Geophysical Monograph Series, A. Levander and G. Nolet (Editors), Vol. **157**, American Geophysical Union, Washington, D.C., 205–227.
- Lee, S. J., B. S. Huang, and W. T. Liang (2006). Grid-based moment tensor inversion by using spectral-element method 3D Green's functions (Abstract S11C-0137), *EOS* **87**, no. 36, (West. Pac. Geophys. Meet. Suppl.), S11C-0137.
- Lin, C. H. (2005). Seismicity increase after the construction of the world's tallest building: an active blind fault beneath the Taipei 101, *Geophys. Res. Lett.* **32**, no. 22, L22313, doi 10.1029/2005GL024223.
- McCulloch, T. H. (1960). Gravity variations and the geology of the Los Angeles basin of California, *U.S. Geol. Surv. Profess. Pap.* **400-B**, 320–325.
- Olsen, K. B. (2000). Site amplification in the Los Angeles basin from three-dimensional modeling of ground motion, *Bull. Seismol. Soc. Am.* **90**, S77–S94.
- Olsen, K. B., R. J. Archuleta, and J. R. Matarese (1995). Three-dimensional simulation of a magnitude 7.75 earthquake on the San Andreas fault, *Science* **270**, 1628–1632.
- Olsen, K. B., J. C. Pechmann, and G. T. Schuster (1996). An analysis of simulated and observed blast records in the Salt Lake basin, *Bull. Seismol. Soc. Am.* **86**, 1061–1076.
- Patera, A. T. (1984). A spectral element method for fluid dynamics: laminar flow in a channel expansion, *J. Comp. Phys.* **54**, 468–488.
- Robertsson, J. O. A. (1996). A numerical free-surface condition for elastic/viscoelastic finite-difference modeling in the presence of topography, *Geophysics* **61**, 1921–1934.
- Stidham, C., M. P. Süß, and J. H. Shaw (2001). 3D density and velocity model of the Los Angeles basin, in *Geological Society of America 2001 Annual Meeting Abstracts*, Vol. **33**, Geological Society of America, Denver, Colorado, 299.
- Wald, D. J., and R. W. Graves (1998). The seismic response of the Los Angeles basin, California, *Bull. Seismol. Soc. Am.* **88**, 337–356.
- Wang, C. Y., Y. H. Lee, M. L. Ger, and Y. L. Chen (2004). Investigating subsurface structures and *P*- and *S*-wave velocities in the Taipei basin, *TAO* **15**, 222–250.
- Wen, K. L., and H. Y. Peng (1998). Site effect analysis in the Taipei basin: results from TSMIP network data, *TAO* **9**, 691–704.
- Wen, K. L., L. Y. Fei, H. Y. Peng, and C. C. Liu (1995). Site effect analysis from the records of the Wuku downhole array, *TAO* **6**, 285–29.
- Yalcinkaya, E., and O. Alptekin (2005). Contributions of basin-edge-induced surface waves to site effect in the Dinar basin, southwestern Turkey, *Pure Appl. Geophys.* **162**, 931–950.

Institute of Earth Sciences
Academia Sinica
Nankang, Taipei 115, Taiwan, Republic of China
sjlee@earth.sinica.edu.tw
hwbs@earth.sinica.edu.tw
(S.-J.L., B.-S.H.)

Institute of Geophysics
National Central University
Jung-Li 320, Taiwan, Republic of China
hwchen@earth.ncu.edu.tw
(H.-W.C.)

Seismological Laboratory
California Institute of Technology
Pasadena, California
lqy@gps.caltech.edu
jtromp@gps.caltech.edu
(Q.L., J.T.)

Department of Geophysical Modeling and Imaging in Geosciences
CNRS UMR 5212 and INRIA Magique 3D
University of Pau
France
(D.K.)

Manuscript received 23 February 2007